Journal of Materials Science & Technology 93 (2021) 221–231

Contents lists available at ScienceDirect

Journal of Materials Science & Technology

journal homepage: www.elsevier.com/locate/jmst

Research Article

# Microstructural refinement mechanism and its effect on toughness in the nugget zone of high-strength pipeline steel by friction stir welding

R.H. Duan[a], G.M. Xie[a,*], P. Xue[b], Z.Y. Ma[b], Z.A. Luo[a], C. Wang[c], R.D.K. Misra[d], G.D. Wang[a]

[a] State Key Laboratory of Rolling and Automation, Northeastern University, No. 3 Wenhua Road, Shenyang 110819, China
[b] Shi-changxu Innovation Center for Advanced Materials, Institute of Metal Research, Chinese Academy of Sciences, 72 Wenhua Road, Shenyang 110016, China
[c] School of Metallurgy, Northeastern University, No. 3 Wenhua Road, Shenyang 110819, China
[d] Department of Metallurgical, Materials, and Biomedical Engineering, University of Texas at El Paso, TX 79968, USA

ARTICLE INFO

*Article history:*
Received 31 January 2021
Revised 23 March 2021
Accepted 8 April 2021
Available online 10 May 2021

*Keywords:*
Pipeline steel
Friction stir welding
Grain refinement
M-A constituent
Toughness

ABSTRACT

High-strength pipeline steel was subjected to friction stir welding (FSW) at rotation rates of 400–700 rpm, and the grain refinement mechanism of the nugget zone (NZ) was determined. The thermo-mechanical process during FSW in the NZ was simulated by multi-pass thermal compression, thereby achieving the austenitic non-recrystallization temperature ($T_{nr}$). The austenitic non-recrystallization in the NZ at the lowest rotation rate of 400 rpm caused a significant grain refinement. Furthermore, the reduced rotation rate also resulted in the formation of a high ratio of island-like martensite-austenite (M-A) constituent. The toughness of the NZs was enhanced as the rotation rate decreased, which is attributed to the fine effective grains and homogeneously distributed fine M-A constituents dramatically inhibiting crack initiation and propagation.



## 1. Introduction

With the rapid development of the economy, the demand for energy has been increasing remarkably. For convenient transport of oil and gas, high strength and high toughness pipeline steel is most often used [1–3]. At present, the pipelines are mainly welded by fusion welding technologies, including submerged arc welding (SAW) and gas metal arc welding (GMAW) [4–6]. Generally, a coarse-grained heat affected zone (CGHAZ) is formed in the vicinity of the fusion line of the pipeline steel joint. For multi-pass welding, a partial CGHAZ, referred as the inter-critically reheated CGHAZ (ICCGHAZ), experiences multiple thermal cycles at the peak temperatures occurring between the start and finish transformation temperatures of austenitic phase ($A_{c1}$ and $A_{c3}$). As a result, the toughness of the ICCGHAZ significantly deteriorates due to the coarse network-like martensite-austenite (M-A) constituents distributed along the prior-austenite grain (PAG) boundaries via the multiple partitioning and diffusing of carbon into the M-A constituents in the dual-phase region [7–9]. Li et al. [10] have carried out double-pass SAW of X100 pipeline steel, and found that the toughness of the ICCGHAZ is only 27.8% of the basal metal (BM) because of the coarse M-A constituents. Therefore, the traditional fusion welding process generates M-A constituents in the ICCGHAZ that are quite coarse due to the multi-pass welding with high heat input, leading to a significant decrease in the toughness of the joint [7–11].

Friction stir welding (FSW) is a solid-state joining technique [12]. Currently, the several inherent issues of FSW have been insightfully pointed out by Meng et al. [13], especially the metallurgical bonding mechanism in the NZ needs to be solved urgently. In comparison with fusion welding, FSW can retard the coarsening of both grains and M-A constituents in the HAZ due to the low peak temperature and fast post-welding cooling rate, thereby improving strength and toughness of the HAZ [14,15]. Recently, FSW has been used to join the pipeline steel. In contrast to the NZ of FSW non-ferrous metal, that of FSW steel exhibits a coarser microstructure in the entire weld because of its high melting point and resistance to deformation. Therefore, more studies have focused on the microstructural refinement and its mechanism in the NZ of FSW steel. Wei and Nelson [16] suggest that the peak temperature of FSW X65 steel decreases from $>>A_{c3}$ to ~$A_{c3}$ by controlling the heat input with a fine ~0.65 $\mu$m wide bainite lath. Xue et al. [17] further point out that the peak temperature located in the dual-phase region is achieved in FSW X80 steel by introducing water cooling, producing a fine dual-phase of a ~0.2 $\mu$m wide martensite lath and ferrite. However, many studies on microstructural refinement have considered phase transformation behavior, but the influence of the

* Corresponding author.
*E-mail address:* xiegm@ral.neu.edu.cn (G.M. Xie).

https://doi.org/10.1016/j.jmst.2021.04.008
1005-0302/

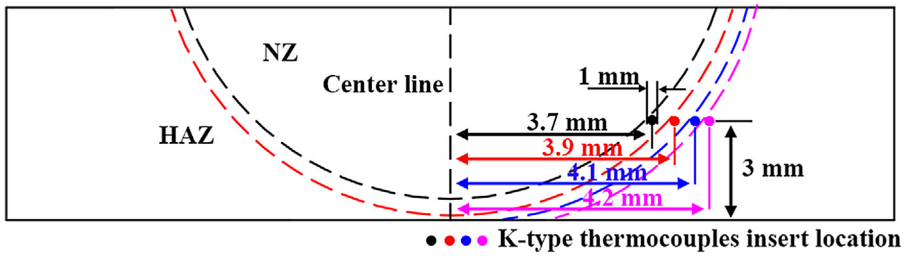


**Fig. 1.** K-type thermocouples insert location during FSW process.

dynamic recrystallization (DRX) process generally was ignored during thermal deformation.

During FSW of bainitic pipeline steel, the complicated thermal cycle and severe plastic deformation has a significant effect on the volume ratio, size, and morphology of the M-A constituent. Santos et al. [18] identified that the morphology of the M-A constituent changed from blocky to slender in the NZ of FSW pipeline steel when the rotation rate of the tool increased. Xie et al. [19] noted that the ratio of fine island-like M-A constituents greatly increased in the NZ of a FSW X80 steel joint after post-welding water cooling was adopted. Irrespective of the above studies, there are few studies on the common effect of peak temperature, plastic deformation, and post-welding cooling rate on the M-A constituent and toughness of the weld joint.

In the present study, a high-strength bainitic pipeline steel was subjected to FSW at different rotation rates, and we studied the austenitic DRX behavior at various peak temperatures, from much higher than the $A_{c3}$ to slightly higher than the $A_{c3}$ regions. By changing the peak temperature, plastic deformation, and cooling rate, the M-A constituents with different characteristics were also analyzed. Furthermore, we evaluated and discussed the mechanism of microstructural refinement and its influence on toughness of FSW pipeline steel joints.

## 2. Experimental procedure

6 mm thick high-strength bainitic pipeline steel plates (450 MPa grade) were used with a chemical composition of Fe-0.07C-0.3Si-1.5Mn-0.05Nb-0.02Ni (wt.%). FSW pipeline steels were conducted at different rotation rates of 700, 600, 500, and 400 rpm with a constant welding speed of 100 mm/min. During the welding process, the tool tilt angle was set at 3° from the nominal direction of the plate, and the plunge depth of the shoulder was 0.2 mm. A W-*Re* tool (W-25Re, wt.%) consisted of a concave shoulder of 15 mm in diameter and a 5 mm length tapered thread pin with 9 mm root diameter and 6 mm tip diameter.

The thermal cycle history profiles in the NZs were measured using K-type thermocouples and an LR8431–30 acquisition instrument, and the thermocouple was inserted into a blind hole drilled from the back of the welded plate. The thermocouple was embedded in the region adjacent the rotating pin, where the thermocouple was not destroyed by the tool, but moved slightly due to the metal flow. In order to determine this region, several blind holes with different distances from the weld center were drilled. The thermal cycle history profiles of NZs at 400, 500, 600, and 700 rpm were measured by the thermocouples inserted at 3.7, 3.9, 4.1, and 4.2 mm from the weld center, respectively, as shown in Fig. 1. Furthermore, the peak temperature can be accurately measured by the telemetry measurement system (MegaStir Technologies, USA) because the rotating thermocouple is quite close to the NZ [20]. Thus, the telemetry system was used to an assistant tool to correct the peak temperature.

The austenitic non-recrystallization temperatures ($T_{nr}$) at different rotation rates during FSW were simulated by an MMS-200 thermal simulation machine. The specimens were soaked at 1200 °C for 180 s, and then were cooled to 1100 °C at a cooling rate of 5 °C/s. Subsequently, specimens were multi-pass compressed from 1100 to 830°C with a constant temperature interval of 30°C between successive passes under air cooling. During thermal simulation, each pass was carried out at a fixed pass strain of 0.12 with various strain rates of 0.5, 1, 2, and 5 $s^{-1}$. The $A_{c1}$ and $A_{c3}$ critical transformation temperatures were measured by a Formastor-II phase transformation instrument.

The metallographic samples of cross-sectional joints were cut perpendicular to the FSW direction. The microstructure was characterized by a Zeiss Ultra-55 scanning electron microscope (SEM) equipped with electron back-scattered diffractometer (EBSD), and an FEI Tecnai G2 F20 transmission electron microscope (TEM). SEM samples were polished and etched with 4% nital, and EBSD samples were prepared by electro-polishing with 87.5% ethanol solution and 12.5% perchloric acid at 25 V for 25 s. The morphology of the M-A constituent was characterized by $L_{max}$ (maximum length), $W_{max}$ (maximum width), and the $L_{max}/W_{max}$ aspect ratio. Image-pro Plus software was used to measure the volume ratio of the M-A constituents. The Charpy v-notch impact samples of NZs were machined vertical to the FSW direction (Fig. 2(a)), and the dimensions of sample are shown in Fig. 2(b). The impact toughness was tested at 20 and −40 °C.

## 3. Results and discussion

### *3.1. Recrystallization process in the NZ*

In the bainitic steel, the grains or packets containing boundaries of misorientation angles ≥ 15° are usually defined as effective grains for the convenience of analysis, which can effectively inhibit crack propagation [21,22]. Fig. 3 shows the effective grains for the BM and NZs at different rotation rates, in which the boundaries corresponding to misorientation angles ≥ 15° and 15° > misorientation angle ≥ 2° are represented by black and yellow lines, respectively. Unlike the BM with elongated grains, the NZ contained equiaxed grains. This is attributed to the fact that FSW, as a severe plastic deformation process, can lead to DRX, and hence an equiaxed microstructure. Furthermore, the effective grain sizes of BM and NZs at 700, 600, 500, and 400 rpm were 6.1, 11.4, 10.8, 9.7, and 6.4 $\mu$m, respectively. The grains of NZs were clearly refined with decreasing rotation rate. Generally, it is thought that the growth of recrystallized grains is inhibited when the heat input is reduced.

During DRX as a result of the FSW, the deformed (or peak) temperature is an important factor. Therefore, the thermal cycle history of NZs at different rotation rates was measured. The four thermal cycle history curves are drawn in Fig. 4 in a continuous time axis for convenient comparison. The peak temperature of NZs at 700, 600, 500, and 400 rpm were 1026, 993, 969, and 912 °C,

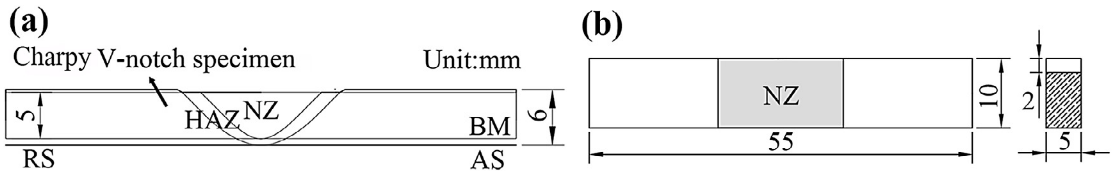


**Fig. 2.** Location and geometric dimensions of Charpy v-notch specimens.

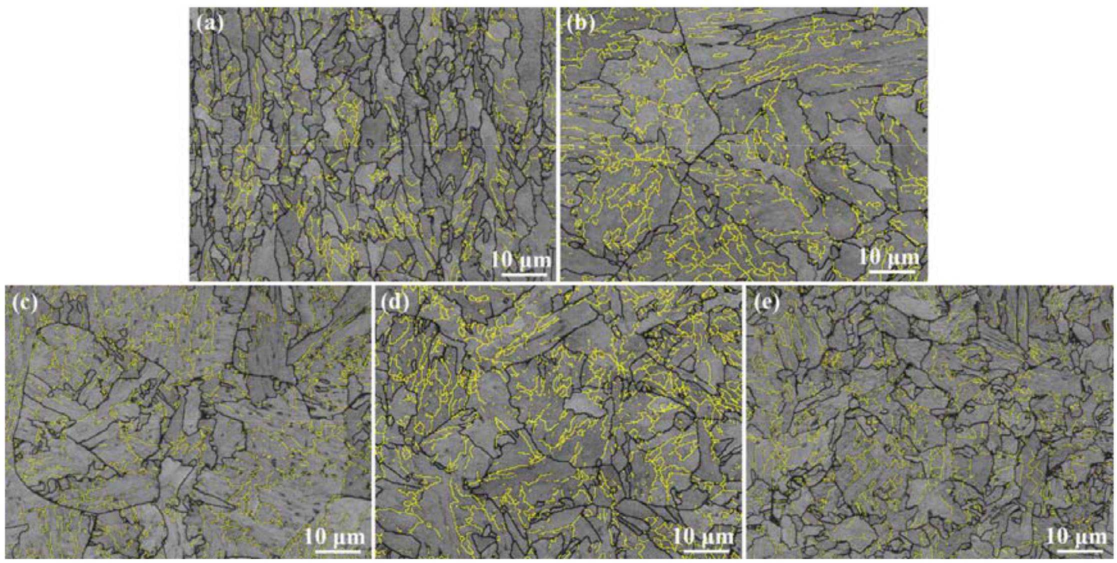


**Fig. 3.** Distribution maps of effective grains of BM and NZs at different rotation rates. (a) BM, (b) 700 rpm, (c) 600 rpm, (d) 500 rpm, and (e) 400 rpm.

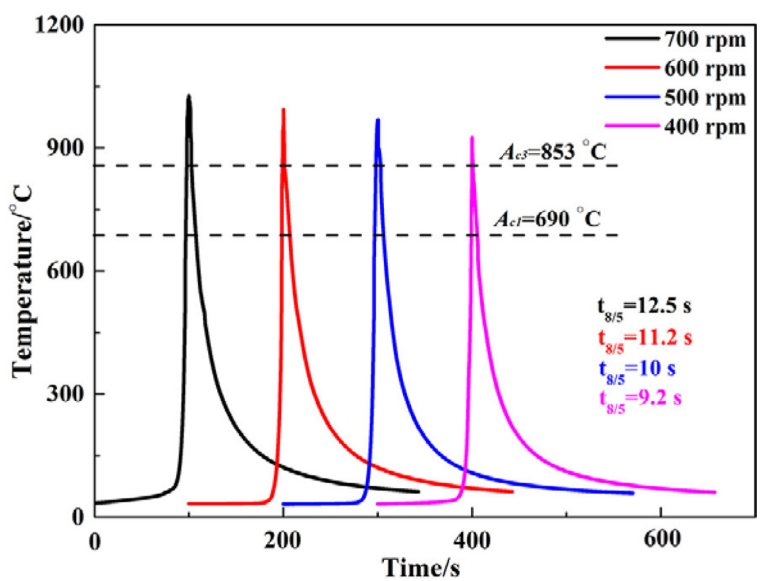


**Fig. 4.** FSW thermal cycle histories of NZs at different rotation rates.

respectively. The peak temperature of NZs decreased with the decrease in rotation rate. The $A_{c1}$ and $A_{c3}$ were measured to be 690 and 853 °C, respectively. Therefore, the peak temperatures at 400–700 rpm were higher than $A_{c3}$, such that the NZ was expected to be completely austenitized. The average cooling time, $t_{8/5}$ (from 800 to 500 °C) at 700, 600, 500, and 400 rpm was 12.5, 11.2, 10, and 9.2 s, respectively, meaning that the post-welding cooling rate increased with the decrease in rotation rate.

To study the microstructural refinement mechanism of NZs, the austenitic DRX process was investigated. During FSW of pipeline steel, the DRX is determined by the Zener-Holloman (Z) parameter:

$$Z = \dot{\varepsilon} \exp\left(Q/RT\right) \tag{1}$$

where $T$ is the deformation temperature (K), $\dot{\varepsilon}$ is the strain rate ($s^{-1}$), $R$ is the gas constant (J/(mol·K)), and $Q$ is the deformation activation energy (kJ/mol). Chang et al. [23] proposed a following equation used to calculate the average strain rate in the NZ during

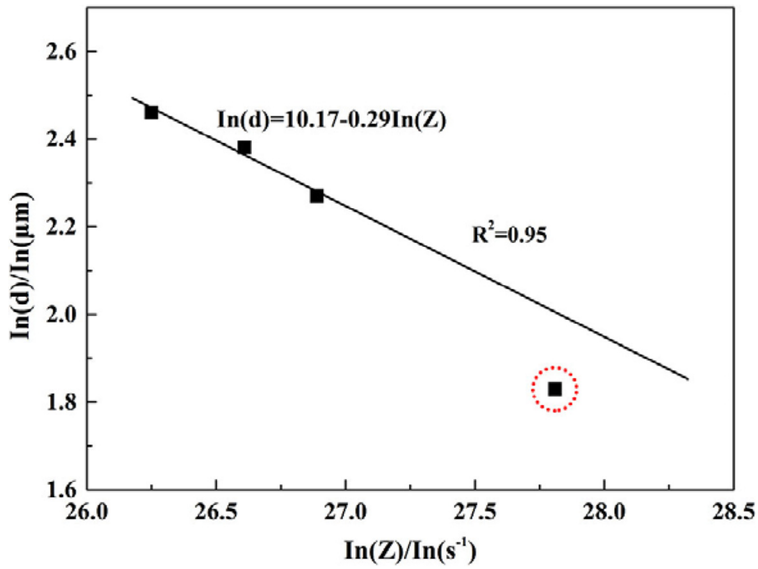


**Fig. 5.** The relationship between effective grain size and Z parameter.

FSW based on the torsion deformation mechanism:

$$\dot{\varepsilon} = \frac{R_{\mathrm{m}} \times 2\pi r_{\mathrm{e}}}{L_{\mathrm{e}}} \tag{2}$$

where $R_m$ is half of the rotation rate (rpm), $r_e$ and $L_e$ are the effective radius and depth of the DRX (mm), which is ~0.78 of the boundary radius and depth of the NZ according to the calculation method of particle average planar radius [24]. The strain rates calculated at 700, 600, 500, and 400 rpm were 28.2, 24.2, 20.1, and 16.1 $s^{-1}$, respectively. The equation for $Q$ (activation energy) that is dependent on the chemical compositions of the steel is [25]:

$$\begin{aligned} Q = {} & 267000 - 2535.52\omega_c + 1010\omega_{\mathrm{Mn}} + 33620.76\omega_{\mathrm{si}} \\ & +35651.28\omega_{\mathrm{Mo}} + 93680.52\omega_{\mathrm{Ti}}^{0.5919} + 31673.46\omega_{\mathrm{V}} \\ & +70729.85\omega_{\mathrm{Nb}}^{0.5649} + 44798.6(\omega_{\mathrm{Ni}} + \omega_{\mathrm{Cu}} + \omega_{\mathrm{Cr}}) \end{aligned} \tag{3}$$

where $\omega$ is the wt.% of chemical composition. The $Q$ of the experimental steel was calculated to be 246.6 kJ/mol. Based on the above result, the fit curve between the Z-parameter and the effective grain size at different rotation rates is shown in Fig. 5. Notably, the DRX grains were refined with an increase of the Z parameter, but the effective grain size at 400 rpm was obviously lower than the fitted value. This abnormal deviation was different from previous studies on the relationship between effective grain and Z parameter [23,26].

For high strength, low-alloy (HSLA) steel, thermo-mechanical processing can be divided into austenitic DRX and non-recrystallization deformations [27,28]. When the austenitic deformation temperature is located in the DRX region, the higher deformation temperature and slower cooling rate produces coarse equiaxed austenite, thereby obtaining a coarse microstructure at ambient temperature. In the $T_{\mathrm{nr}}$ region, the severe plastic deformation causes the formation of pancaked austenite and deformation bands, which subsequently transform into a fine microstructure during cooling. Based on these observations, the abnormal refinement of effective grains at 400 rpm may be related to the austenitic non-recrystallization, such that determining $T_{\mathrm{nr}}$ is necessary to unravel the mechanism of microstructural refinement. An earlier study determined that $T_{\mathrm{nr}}$ can be measured by multi-pass compression thermal simulation [29]. Fig. 6 shows the stress-strain curve of ten-pass compression at different strain rates of 0.5, 1, 2, and 5 $s^{-1}$. The mean flow stress (MFS) was defined as the integral area under each stress-strain curve divided by the pass strain [29,30]. The variation of MFS corresponding to each pass with inverse deformation temperature is plotted in Fig. 7, where $T_{\mathrm{nr}}$ was determined from the intersection between the two regression lines. The $T_{\mathrm{nr}}$ at different strain rates of 0.5, 1, 2, and 5 $s^{-1}$ were 1000, 990, 983, and 977 °C, respectively. Note that $T_{\mathrm{nr}}$ during FSW cannot be directly obtained via thermal simulation because the high strain rate of $\geq$ 16.1 $s^{-1}$ exceeded the maximum strain rate capability of the thermal simulation equipment at 10 $s^{-1}$. To achieve $T_{\mathrm{nr}}$ at a higher strain rate, the experimental data in Fig. 7 (a–d) were fit to the following equation:

$$T_{\mathrm{nr}} = 991.45\dot{\varepsilon}^{-0.01} \tag{4}$$

The $T_{\mathrm{nr}}$ values at 16.1, 20.1, 24.2, and 28.2 $s^{-1}$ corresponding to 400, 500, 600, and 700 rpm were 964.3, 962.1, 960.4, and 958.9 °C, respectively. Therefore, the peak temperature at a rotation rate of $\geq$ 500 rpm was higher than $T_{\mathrm{nr}}$, while the peak temperature of NZ at 400 rpm was lower than $T_{\mathrm{nr}}$. Also, the austenitic DRX occurred in the NZ at $\geq$ 500 rpm, while austenitic non-recrystallization occurred at 400 rpm. Although previous studies reported that quite fine grains were found in the NZ of FSW low-alloy steels at peak temperatures just higher than $A_{c3}$, no detailed explanation was given [20,27].

For the HSLA steel, the deformation severely influenced the phase transformation during cooling. Thus, EBSD and TEM analyses on the NZs at 600 and 400 rpm were conducted. The inverse pole figures (IPF) and TEM images are shown in Fig. 8. At the higher heat input of 600 rpm, the peak temperature of $>T_{\mathrm{nr}}$ and strong deformation produced coarse austenitic DRX grains. During cooling, ferrite preferentially nucleated at the PAG boundaries, and then grew into the grain interior, as shown in Fig. 8(a). Meanwhile, it was further determined that at 600 rpm, fine ferrites containing a low dislocation density was formed at the PAG boundaries (Fig. 8(b)). At the lower heat input of 400 rpm, there was non-recrystallization in austenite because of the low peak temperature of $<T_{nr}$. Ferrite nucleated simultaneously at grain boundaries and in the grain interior (Fig. 8(c)), which is attributed to the higher dislocation density in austenite, leading to more ferritic nucleation sites [31,32]. The TEM results also show that bainitic ferrite was distributed at PAG boundaries and in the interior of the grain (Fig. 8(d)).

Based on the above analyses, austenitic DRX and non-recrystallization models are schematically illustrated in Fig. 9. At

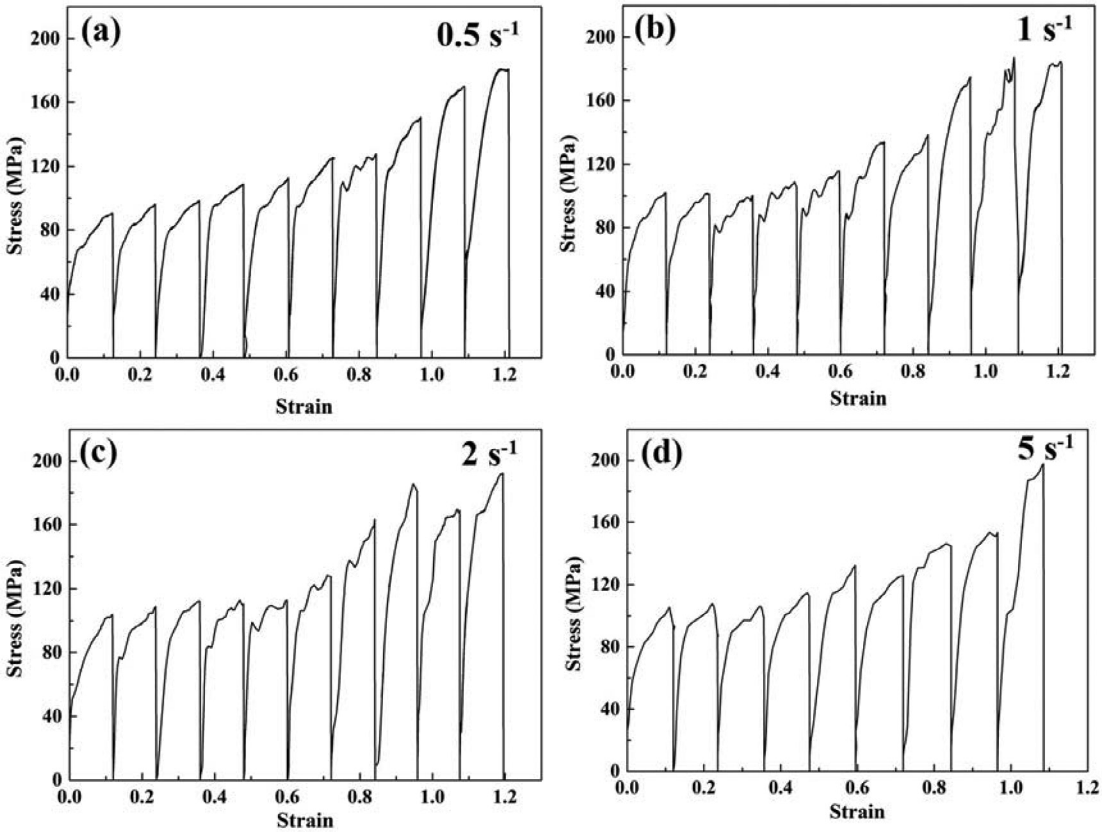


**Fig. 6.** Stress-strain curves of multi-pass thermal compression at different strain rates. (a) 0.5 $s^{-1}$, (b) 1 $s^{-1}$, (c) 2 $s^{-1}$, and (d) 5 $s^{-1}$.

deformation temperatures $>T_{nr}$, the severe deformation of the austenite elongated the grains, forming many dislocations and substructures in the austenite. Meanwhile, the cross slip and climb of dislocations at elevated temperatures promoted annihilation and rearrangement of dislocations, producing a number of sub-grains. In this case, adjacent sub-grains with lower misorientation angles began to rotate and coalesce to reduce stored energy, forming new DRX grains. During the subsequent cooling transformation, the PAG boundaries provided heterogeneous nucleation sites because of their high energy and activity [31,32]. Therefore, ferrite nucleated preferentially at the PAG boundaries, and grew into interior grains, finally forming bainitic ferrite. At lower deformation temperatures $\leq T_{nr}$, the work-hardened austenite was elongated, and a large amount of dislocations and substructures accumulated and were entangled in the deformed austenite, providing a large number of sites for ferrite nucleation. During the subsequent cooling, the ferrite nucleated at the austenite boundaries and in the interior of the grains, and finer bainitic ferrite formed during the fast cooling rate.

### *3.2. Characteristics of M-A constituent in the NZs*

Usually, the carbon content in pipeline steel is relatively low to ensure excellent toughness. Therefore, a majority of the carbon in the pipeline steel is present in the M-A constituent without the occurrence of cementite, and the effects of volume ratio, size, and morphology of the M-A constituent on toughness is complex [21,33].

SEM micrographs of the BM and NZs at 600 and 400 rpm are shown in Fig. 10. The BM predominantly consisted of a large amount of fine acicular ferrite (AF) and island-like M-A constituents (Fig. 10(a)). Bainitic ferrite and M-A constituents exhibited a variety of morphologies in the NZs at various rotation rates. At 600 rpm, numerous coarse bainitic ferrite phases were apparent, with a uniform distribution of blocky M-A constituents (Fig. 10(b)). The elevated temperature and slow cooling rate at 600 rpm were conducive to the formation of blocky M-A constituents because of sufficient carbon partitioning. At 400 rpm, a number of lath bainite (LB) phases were detected in the NZ with a large amount of slender M-A constituents distributed along LB boundaries (Fig. 10(c)). At the low peak temperature and fast cooling rate conditions, the displacive transformation phase of LB formed, and then the carbon atoms within the laths diffused near the lath boundaries, forming slender M-A constituent grains. Clearly, the microstructural feature of bainitic ferrite and M-A constituent during FSW low-alloy steel was affected by peak temperature, plastic deformation, and cooling rate.

The M-A constituents were carefully characterized by TEM and EBSD, as shown in Fig. 11. From the TEM images, twin martensite appeared in blocky and slender M-A constituents, besides the retained austenite. Retained austenite at the periphery of the M-A constituent had a higher carbon content, thereby exhibiting higher stability, which was attributed to the slow diffusion of carbon and the austenitic volume constraint at the $\alpha/\gamma$ interface [34]. The volume ratio of the M-A constituent in the NZs at 600 and 400 rpm measured from Fig. 10 were 15.2 and 12.3%, respectively, indicating that the high peak temperature at 600 rpm promoted partitioning and diffusion of carbon, thereby forming the coarse M-A constituent. The red regions represent retained austenite in Fig. 11(a, c), and their volume ratios at 600 and 400 rpm were 0.10 and 0.22%, respectively. Further, the volume ratio of austenite to martensite at 600 and 400 rpm were 0.7% and 1.8%, respectively. Obviously, at 600 rpm the higher ratio of prior-austenite was transformed to twin martensite during post-weld cooling. By com-

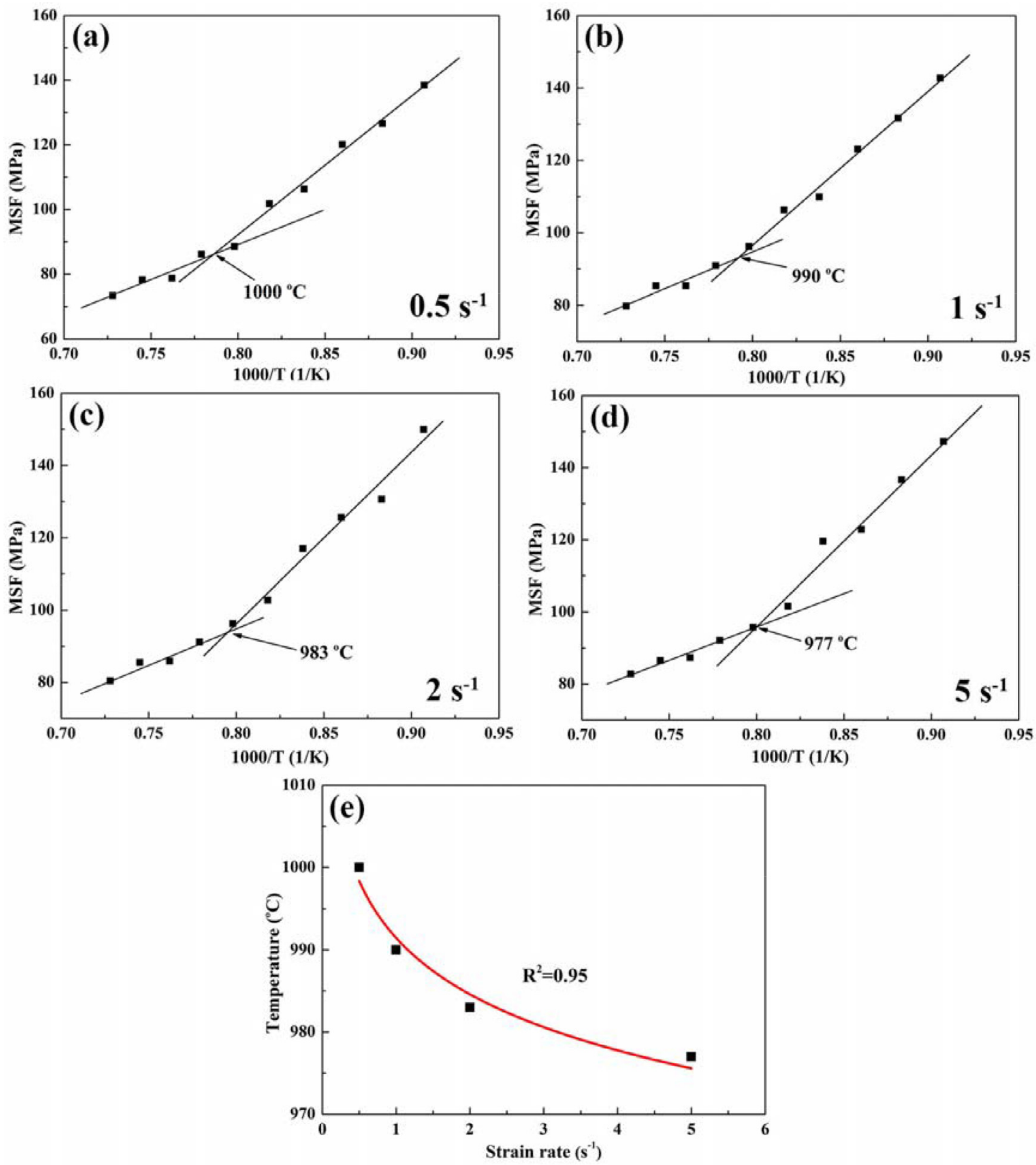


**Fig. 7.** MFS vs 1000/T plot at different strain rates. (a) 0.5 $s^{-1}$, (b) 1 $s^{-1}$, (c) 2 $s^{-1}$, (d) 5 $s^{-1}$, and (e) fitted curve.

parison, the average concentration of carbon in prior austenite at 600 rpm was lower because of the higher ratio of the M-A constituent. Therefore, at 600 rpm, the austenite exhibited poor stability, thereby resulting in the low austenite/martensite ratio.

### 3.3. The effect of microstructure on the toughness of NZs

The impact toughness values of BM and NZs at 400 and 600 rpm are shown in Fig. 12. The low-temperature toughness at −40 °C obtained at 600 and 400 rpm reached 87.6 and 101% of the BM, respectively. The toughness of the NZ induced by FSW was superior compared to that of SAW for the same pipeline steel, because of the relatively low heat input of FSW [3].

It is well known that grain refinement is a unique mechanism that improves strength and toughness simultaneously. The brittle fracture stress is directly related to the effective grain size according to the fracture strength theory equation [35,36]:

$$\sigma_B = \sqrt{\frac{2}{\pi L}} K_{Ic} \propto \frac{1}{\sqrt{d}} \tag{6}$$

where $\sigma_B$ is the brittle fracture stress, $K_{Ic}$ is the fracture toughness, $L$ is the characteristic length of brittle failure, and $d$ is effective grain size. The brittle fracture stress increased with the decrease in effective grain size, which is attributed to the high ratio of effective grain boundaries arresting the propagation of cleavage microcracks [36]. Moreover, the high-angle boundaries inhibited straight propagation of cracks and consumed more energy, eventually increasing the toughness. Therefore, the toughness of NZs at 400 rpm was enhanced by decreasing the effective grain size.

Furthermore, according to Griffith theory, the brittle and hard M-A constituent can be regarded as a defect, such that the microcrack formed and propagated near the interface between the M-A constituent and the matrix, when the stress concentration around the M-A constituent exceeded the critical cracking stress [37,38].

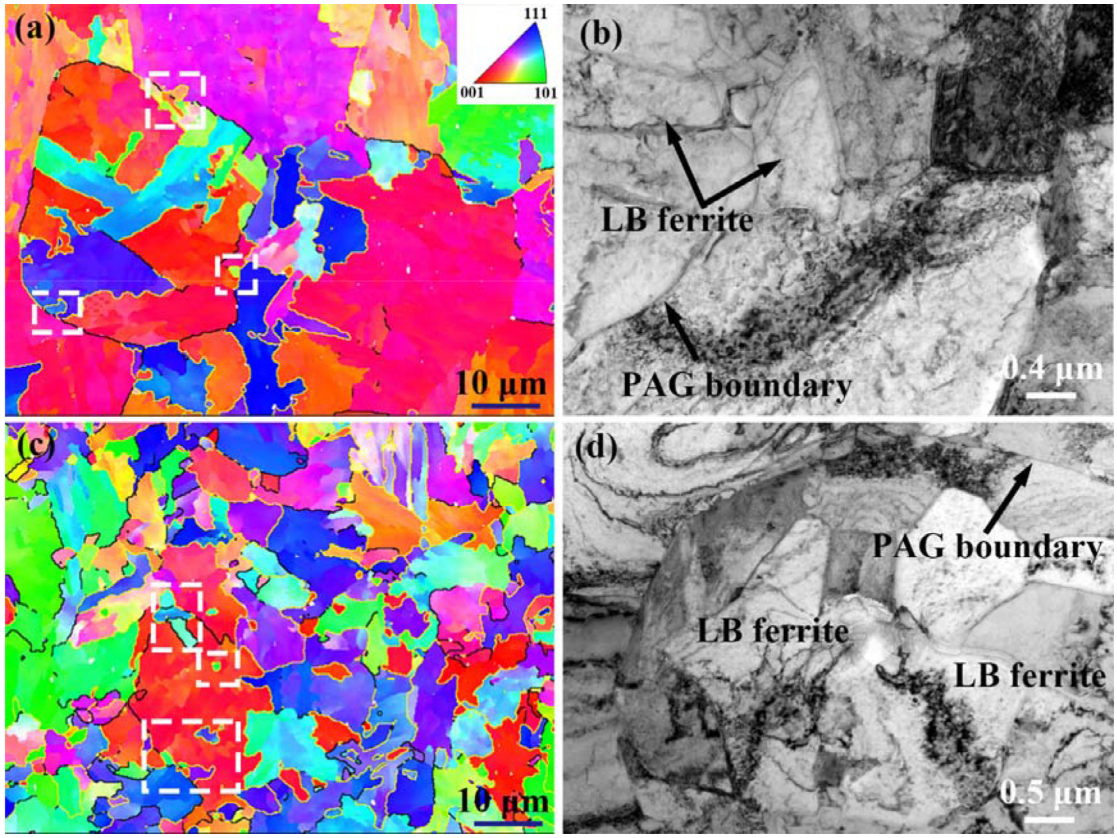


**Fig. 8.** IPF maps and TEM images of NZs at different rotation rates. (a, b) 600 rpm and (c, d) 400 rpm.

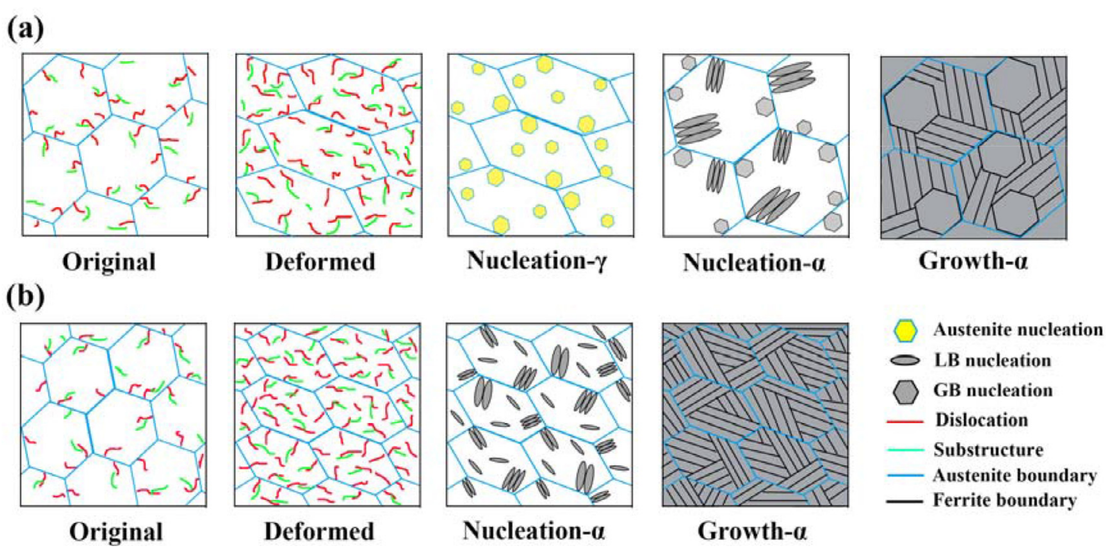


**Fig. 9.** Schematic illustration of mechanism of recrystallization and non-recrystallization of austenite. (a) Austenite DRX, (b) Austenite non-recrystallization.

The Griffith equation is given by the following:

$$\sigma_c = \left( \frac{\pi E \gamma_p}{(1 - \nu^2) D} \right)^{1/2} \tag{7}$$

where $\sigma_c$ is the critical cracking stress, $\gamma_p$ is the effective surface energy of microcrack, $\nu$ is the Poisson's ratio, $E$ is the Young's modulus, and $D$ is the length of the critical crack. Here, $D$ can be regarded as the $W_{max}$ of the M-A constituent. The $W_{max}$ of the M-A constituent at 600 and 400 rpm was 1.44 and 0.97 $\mu$m, respectively, and the corresponding $\sigma_c$ was 2668 and 3234 MPa, respectively. Therefore, a high $\sigma_c$ for fine island-like M-A constituent renders formation of microcracks difficult, and the secondary crack initiation is also arrested, thereby consuming more crack propagation energy.

The crack propagation paths at 400 and 600 rpm are revealed in Fig. 13. At 600 rpm, no obvious deformation appeared during crack propagation because of the coarse, slender M-A constituent containing the high ratio of twin martensite. Meanwhile, the crack initiated at the interface between the blocky M-A constituents and the matrix (Fig. 13(b)), likely due to the intense stress concentration present at the interface. Thus,

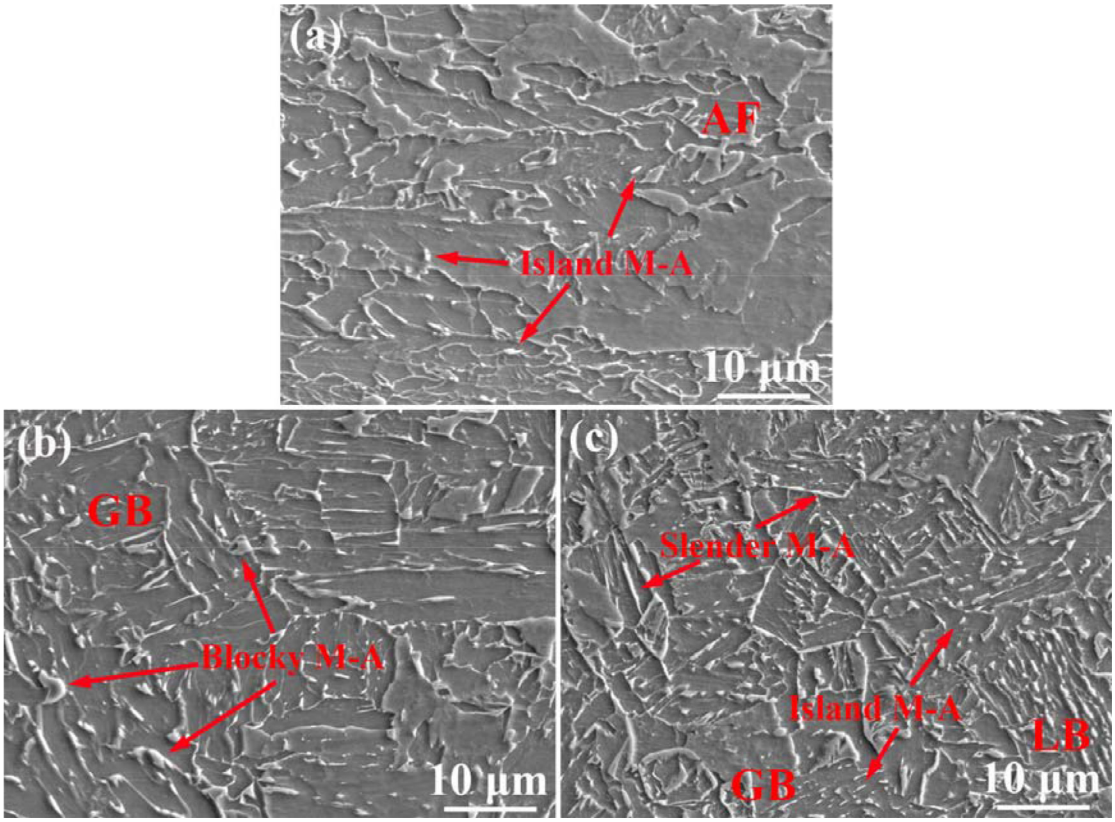


**Fig. 10.** SEM micrographs of BM and NZs at different rotation rates. (a) BM, (b) 600 rpm, and (c) 400 rpm.

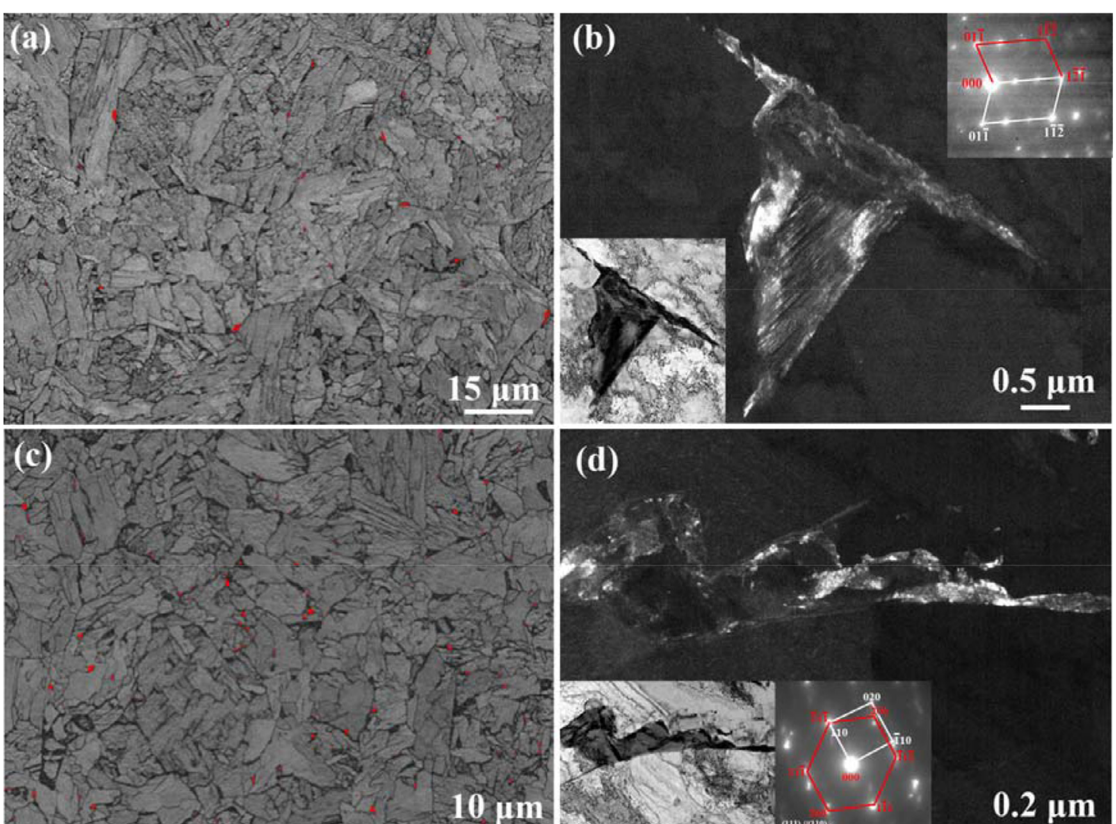


**Fig. 11.** SEM and TEM micrographs of NZs at different rotation rates. (a, b) 600 rpm and (c, d) 400 rpm.

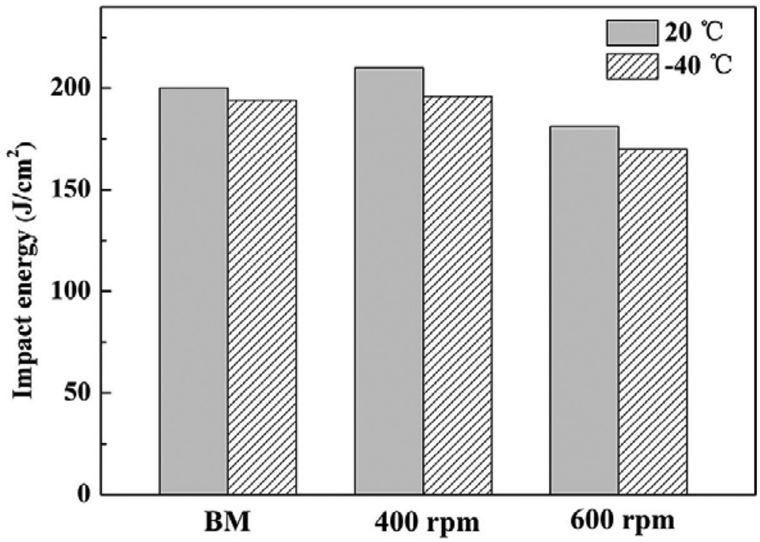


**Fig. 12.** Impact energy of BM and NZs at different rotation rates.

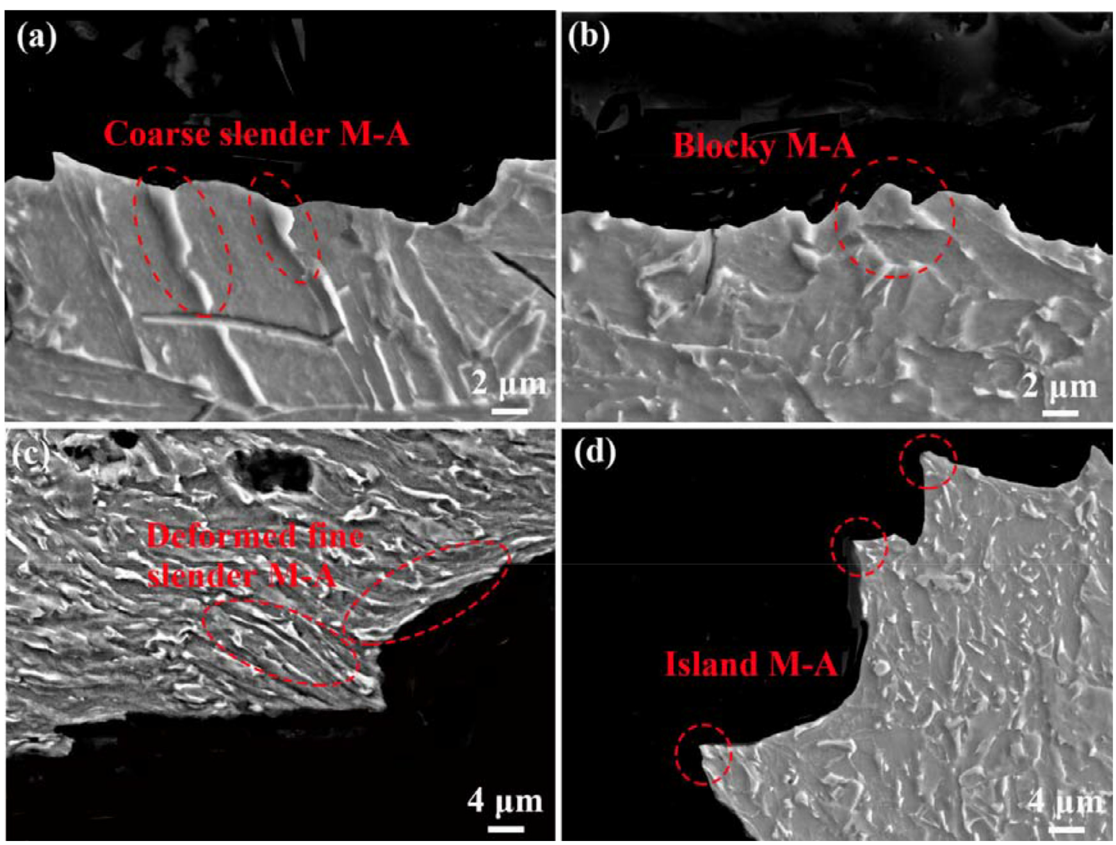


**Fig. 13.** SEM micrographs of crack propagation path in the NZs at different rotation rates. (a, b) 600 rpm and (c, d) 400 rpm.

the toughness of the NZ at 600 rpm decreased. At 400 rpm, the fine slender M-A constituents underwent plastic deformation during crack propagation, which implies that the part of crack propagation energy can be consumed by the plastic deformation. Additionally, the higher $\sigma_c$ for the island-like M-A constituents effectively arrested the crack growth and caused zigzag crack growth paths (Fig. 13(d)). Therefore, the fine slender and island-like M-A constituents hindered crack growth, enhancing toughness.

For a detailed analysis of the influence of the M-A constituent morphology on toughness, M-A constituents typically can be classified into I, II, III, and IV types, as shown in Fig. 14. The four types consist of the island-like M-A constituents ($L_{max}$ < 3 $\mu$m, aspect ratio < 3), fine slender M-A constituents ($L_{max}$ <3 $\mu$m, aspect ratio > 3), coarse slender M-A constituents ($L_{max}$ > 3 $\mu$m, aspect ratio > 3), and blocky M-A constituents ($L_{max}$ >3 $\mu$m, aspect ratio < 3), respectively. At 600 rpm, the high ratio of coarse slender (18.4%) and blocky M-A (18%) constituents can create an obvious stress concentration, which is an important reason for the lower toughness. At 400 rpm, the high ratio of fine slender (30.4%) and island-like (57.9%) M-A constituents significantly increased the toughness.

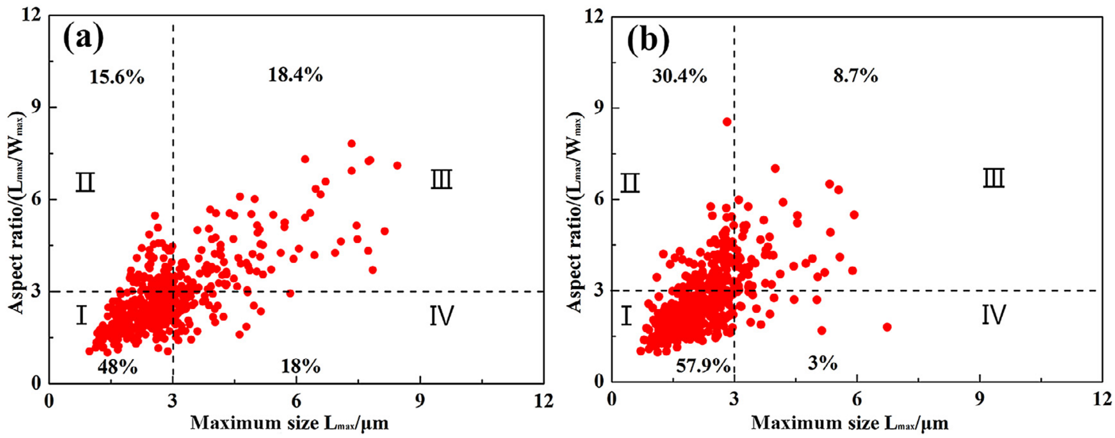


**Fig. 14.** Distribution characteristics of M-A constituent of NZs at different rotation rates (I, II, III, and IV regions represent island-like, fine slender, coarse slender, and blocky M-A constituents, respectively.) (a) 600 rpm and (b) 400 rpm.

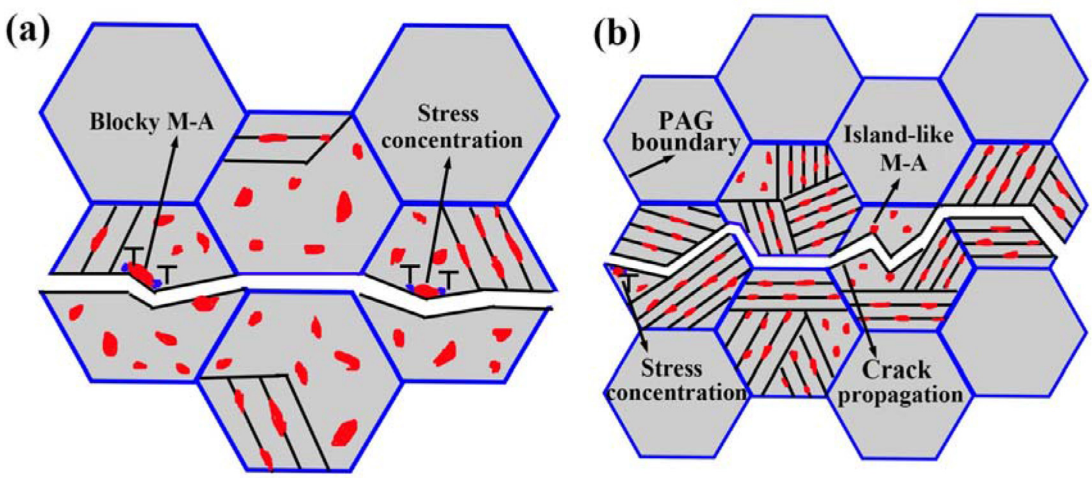


**Fig. 15.** Schematic diagram of ductile fracture and cleavage fracture. (a) Cleavage fracture, (b) Ductile fracture.

Based on a study of the fracture behavior of FSW bainitic pipeline steel, the brittle and ductile crack propagation models are summarized in Fig. 15. At the high heat input condition, the coarse effective grains resulted in lower $\sigma_B$, which significantly promoted the brittle fracture and decreased toughness. In addition, the microcracks initiated readily between the coarse blocky M-A constituent and the matrix due to the lower $\sigma_c$ and propagated easily across the blocky M-A constituent. Therefore, a shorter crack propagation path was revealed in Fig. 15(a), which consumed less energy. At the low heat input condition, the effective grains obviously refined by non-recrystallization when welded by FSW contributed to a higher $\sigma_B$ that significantly inhibited brittle fracture. Meanwhile, the higher $\sigma_c$ made the microcrack initiation difficult due to the small island-like M-A constituents, and fine M-A constituents can deflect the propagated cracks. Therefore, a longer and zigzag propagation path that consumed more energy was evident in Fig. 15(b). Based on our study, FSW carried out in a non-recrystallization region can effectively improve the toughness in the NZ.

## 4. Conclusions

(1) The austenitic DRX appeared in the NZs at rotation rates of ≥500 rpm, while austenitic non-recrystallization occurred at 400 rpm. The effective grain size in the NZ at 400 rpm was obviously refined because ferrite simultaneously nucleated at grained boundaries and within the grains.
(2) With the decrease in rotation rate, the volume ratio of the M-A constituents was reduced, and the M-A constituents were significantly refined and transformed from blocky to island-like phases. The austenite/martensite ratio of the NZs at 600 and 400 rpm was estimated to be 0.7%, and 1.8%, respectively.
(3) The toughness of the NZs was enhanced by the decreasing rotation rate, and the low-temperature toughness at −40 °C reached 87.6 and 101% of the BM at 600 and 400 rpm, respectively.
(4) By means of controlling the peak temperature of FSW steel at the austenitic non-recrystallization region, the resistance to deformation during FSW was not high and the toughness of the NZ also was improved, which has a certain significance to prolong the tool life.

## Declaration of Competing Interest

The authors declare that they have no known competing financial interests or personal relationships that could have appeared to influence the work reported in this paper.

## Acknowledgments

This work was supported by the National Nature Science Foundation of China (No. 51774085), Liaoning Province Excellent Youth Foundation (2020-YQ-03), and the Open Research Fund from the State Key Laboratory of Rolling and Automation, Northeastern University (NEU) (2020RALKFKT009). The authors also are grateful to the financial auspices of the NEU innovation team and Professor R.D.K. Misra for continued collaboration with NEU.

## References

[1] J. Li, X.H. Gao, L.X. Du, Z.G. Liu, J. Mater. Sci. Technol. 33 (2017) 1504–1512.
[2] J.B. Ju, W.S. Kim, J.I. Jang, Mater. Sci. Eng. A 546 (2012) 258–262.
[3] S.H. Hashemi, D. Mohammadyani, Int. J. Press. Vessel. Pip. 98 (2012) 8–15.
[4] A.R.H. Midawi, E.B.F. Santos, N. Huda, A.K. Sinha, R. Lazor, A.P. Gerlich, J. Mater. Process. Technol. 226 (2015) 272–279.
[5] A.R.H. Midawi, C.H.M. Simha, A.P. Gerlich, Int. J. Press. Vessel. Pip. 168 (2018) 258–268.
[6] Y.H. Yang, L. Shi, Z. Xu, H.S. Lu, X. Chen, X. Wang, Eng. Fract. Mech. 148 (2015) 337–349.
[7] X.D. Li, Y.R. Fan, X.P. Ma, S.V. Subramanian, C.J. Shang, Mater. Des. 67 (2015) 457–463.
[8] Z.X. Zhu, L. Kuzmikova, H.J. Li, F. Barbaro, Mater. Sci. Eng. A 605 (2014) 8–13.
[9] V.G. Haugen, B.R.S. Rogne, O.M. Akselsen, C. Thaulow, E. Østby, Mater. Des. 59 (2014) 135–140.
[10] X.D. Li, C.J. Shang, X.P. Ma, S.V. Subramanian, in: Study on the toughness of X100 pipeline steel heat affected zone. Proceedings of the Conference on Energy Materials, Xian, China, November 4-6, 2014.
[11] M. Mohammadijoo, J. Valloton, L. Collins, H. Henein, D.G. Ivey, Mater. Charact. 142 (2018) 321–331.
[12] R.S. Mishra, Z.Y. Ma, Mater. Sci. Eng. R 50 (2005) 1–78.
[13] X.C. Meng, Y.X. Huang, J. Cao, J.J. Shen, J.F.D. Santos, Prog. Mater. Sci. 115 (2021) 1–74.
[14] F.C. Liu, Y. Hovanski, M.P. Miles, C.D. Sorensen, T.W. Nelson, J. Mater. Sci. Technol. 34 (2018) 39–57.
[15] W. Wang, P. Han, P. Peng, T. Zhang, Q. Liu, S.N. Yuan, L.Y. Huang, H.L. Yu, K. Qiao, K.S. Wang, Acta Metall. Sin. (Engl. Lett.) 33 (2020) 43–57.
[16] L.Y. Wei, T.W. Nelson, Mater. Sci. Eng. A 556 (2012) 51–59.
[17] P. Xue, B.L. Xiao, W.G. Wang, Q. Zhang, D. Wang, Q.Z. Wang, Z.Y. Ma, Mater. Sci. Eng. A 575 (2013) 30–34.
[18] T.F.A. Santos, T.F.C. Hermenegildo, C.R.M. Afonso, R.R. Marinho, M.T.P. Paes, A.J. Ramirez, Eng. Fract. Mech. 77 (2010) 2937–2945.
[19] G.M. Xie, R.H. Duan, P. Xue, Z.Y. Ma, H.L. Liu, Z.A. Luo, Acta Metall. Sin. (Engl. Lett.) 33 (2020) 88–102.
[20] G.M. Xie, H.B. Cui, Z.A. Luo, W. Yu, J. Ma, G.D. Wang, J. Mater. Sci. Technol. 32 (2016) 326–332.
[21] H.F. Lan, L.X. Du, R.D.K. Misra, Mater. Sci. Eng. A 611 (2014) 194–200.
[22] J. Hu, L.X. Du, J.J. Wang, Mater. Sci. Eng. A 554 (2012) 79–85.
[23] C.I. Chang, C.J. Lee, J.C. Huang, Scr. Mater. 51 (2004) 509–514.
[24] A.J. Ardell, Metall. Trans. A 16 (1985) 2131–2165.
[25] L.Y. Lan, C.L. Qiu, D.W. Zhao, X.H. Gao, L.X. Du, J. Iron. Steel. Res. Int. 18 (2011) 55–60.
[26] K. Dehghani, A. Chabok, Mater. Sci. Eng. A 528 (2011) 4325–4330.
[27] T.F.C. Hermenegildo, T.F.A. Santos, E.A. Torres, C.R.M. Afonso, A.J. Ramirez, Met. Mater. Int. 24 (2018) 1120–1132.
[28] S.Y. Wang, H. Yu, T. Zhou, T. Wang, Mater. Des. 88 (2015) 847–853.
[29] V. Rajinikanth, T. Kumar, B. Mahato, S.G. Chowdhury, S. Sangal, Metall. Mater. Trans. A 50 (2019) 5816–5838.
[30] R. Abad, A.I. Fernandez, B. Lopez, J.M. Rodriguez-Ibabe, ISIJ Int. 41 (2001) 1373–1382.
[31] K. Huang, R.E. Logé, Mater. Des. 111 (2016) 548–574.
[32] Y. Zhou, S.Y. Chen, X.T. Chen, T. Cui, J. Liang, C.S. Liu, Mater. Sci. Eng. A 742 (2019) 150–161.
[33] H.B. Cui, G.M. Xie, Z.A. Luo, J. Ma, G.D. Wang, R.D.K. Misra, J. Alloy. Compd. 681 (2016) 426–433.
[34] A. Lambert, J. Drillet, A.F. Gourgues, T. Sturel, A. Pineau, Sci. Technol. Weld. Join. 5 (2000) 168–173.
[35] J.Q. Xu, in: Theory on the strength of materials, Shanghai Jiao Tong University Press, Shanghai, 2009, pp. 94–98. (in chinese).
[36] J.W. Morris, Science 320 (2008) 1022–1023.
[37] X. Luo, X.H. Chen, T. Wang, S.W. Pan, Z.D. Wang, Mater. Sci. Eng. A 710 (2018) 192–199.
[38] L.Y. Lan, C.L. Qiu, D.W. Zhao, X.H. Gao, L.X. Du, Mater. Sci. Eng. A 529 (2011) 192–200.